# Cation reordering instead of phase transitions: Origins and implications of contrasting lithiation mechanisms in 1D ζ- and 2D α-$V_2O_5$

Yuting Luo[a,b], Shahed Rezaei[c], David A. Santos[a,b], Yuwei Zhang[d], Joseph V. Handy[a,b], Luis Carrillo[a,b], Brian J. Schultz[e], Leonardo Gobbato[e], Max Pupucevski[e], Kamila Wiaderek[f], Harry Charalambous[f], Andrey Yakovenko[f], Matt Pharr[d], Bai-Xiang Xu[c,1], and Sarbajit Banerjee[a,b,1]

[a]Department of Chemistry, Texas A&M University, College Station, TX 77843; [b]Department of Materials Science and Engineering, Texas A&M University, College Station, TX 77843; [c]Institute of Materials Science, Mechanics of Functional Materials, Technische Universität Darmstadt, Darmstadt 64287, Germany; [d]Department of Mechanical Engineering, Texas A&M University, College Station, TX 77843; [e]Dimien Inc., Buffalo, NY 14228; and [f]X-ray Science Division, Argonne National Laboratory, Argonne, IL 60439

Edited by Catherine Murphy, Department of Chemistry, University of Illinois at Urbana–Champaign, Urbana, IL; received August 17, 2021; accepted December 21, 2021

**Substantial improvements in cycle life, rate performance, accessible voltage, and reversible capacity are required to realize the promise of Li-ion batteries in full measure. Here, we have examined insertion electrodes of the same composition ($V_2O_5$) prepared according to the same electrode specifications and comprising particles with similar dimensions and geometries that differ only in terms of their atomic connectivity and crystal structure, specifically two-dimensional (2D) layered α-$V_2O_5$ that crystallizes in an orthorhombic space group and one-dimensional (1D) tunnel-structured ζ-$V_2O_5$ crystallized in a monoclinic space group. By using particles of similar dimensions, we have disentangled the role of specific structural motifs and atomistic diffusion pathways in affecting electrochemical performance by mapping the dynamical evolution of lithiation-induced structural modifications using ex situ scanning transmission X-ray microscopy, *operando* synchrotron X-ray diffraction measurements, and phase-field modeling. We find the operation of sharply divergent mechanisms to accommodate increasing concentrations of Li-ions: a series of distortive phase transformations that result in puckering and expansion of interlayer spacing in layered α-$V_2O_5$, as compared with cation reordering along interstitial sites in tunnel-structured ζ-$V_2O_5$. By alleviating distortive phase transformations, the ζ-$V_2O_5$ cathode shows reduced voltage hysteresis, increased Li-ion diffusivity, alleviation of stress gradients, and improved capacity retention. The findings demonstrate that alternative lithiation mechanisms can be accessed in metastable compounds by dint of their reconfigured atomic connectivity and can unlock substantially improved electrochemical performance not accessible in the thermodynamically stable phase.**

intercalation chemistry | batteries | energy storage | *operando* X-ray diffraction | scanning transmission X-ray microscopy

Li-ion batteries are the mainstay of electrochemical energy storage and are at the forefront of an unprecedented global transition to electromobility (1–5). However, by some accounts, commercial cells currently achieve less than 25% of their theoretical capacity (6, 7). Mitigating the constraints and degradation mechanisms that limit cathode materials from realizing their full potential requires consideration of the dynamical evolution of structure across multiple length scales (8, 9). In this work, we directly interrogate the role of lattice structure by comparing electrochemical lithiation/delithiation mechanisms in two distinct polymorphs of $V_2O_5$, which differ in atomic connectivity but have the same composition (10–13). By using particles of similar dimensions, we seek to disentangle the role of specific structural motifs and atomistic diffusion pathways in each polymorph by mapping the dynamical evolution of lithiation-induced structural modifications using *operando* synchrotron X-ray diffraction (XRD) measurements and ex situ scanning transmission X-ray microscopy (STXM) and by correlating the observed structure evolution to electrochemical performance and the coupling of electrochemistry with mechanics.

α-$V_2O_5$ is a promising cathode material and is the active cathode in small-format commercial cells (14, 15). The promise of this material as an intercalation host stems from the high natural abundance and geographical diversity of vanadium deposits, as well as the existence of well-established approaches for extraction and processing of high-purity vanadium from ores, steel slag, and fly ash. $V_2O_5$ has a high theoretical capacity, potential for multielectron redox (7), and reasonable rate performance. However, cation intercalation in α-$V_2O_5$ brings about a sequence of phase transformations (16, 17). Beyond $x > 1$ in $Li_xV_2O_5$, such structural distortions become irreversible (18–23). Phase heterogeneities inevitably induce coherency strains as a result of lattice mismatch between immiscible low

## Significance

The function of cathode materials is determined by factors transcending decades of length scales, spanning the range from the crystal structure and composition of the compound to the dimensions and morphologies of the particles, their connectivity with other particles and with the conductive matrix, and their spatial location relative to the electrolyte–electrode interface. Mitigating the constraints and degradation mechanisms that limit cathode materials from realizing their full potential requires careful consideration of the electrode structure spanning multiple length scales. In this work, we explore an intriguing concept: For the same exact composition ($V_2O_5$), can the atomic connectivity be altered to stabilize a metastable polymorph that provides access to an entirely distinctive cation insertion and diffusion mechanism?

Author contributions: Y.L., S.R., J.V.H., B.J.S., M. Pharr, B.-X.X., and S.B. designed research; Y.L., S.R., D.A.S., Y.Z., J.V.H., L.C., L.G., M. Pupucevski, K.W., H.C., and A.Y. performed research; B.J.S., K.W., H.C., A.Y., M. Pharr, and B.-X.X. contributed new reagents/analytic tools; Y.L., S.R., D.A.S., Y.Z., J.V.H., L.C., B.J.S., L.G., M. Pharr, B.-X.X., and S.B. analyzed data; and Y.L., S.R., D.A.S., J.V.H., M. Pharr, B.-X.X., and S.B. wrote the paper.

Competing interest statement: B.J.S., L.G., and M. Pupucevski are part of a startup company, Dimien LLC, that is developing cathode technologies.

This article is a PNAS Direct Submission.



[1]To whom correspondence may be addressed. Email: xu@mfm.tu-darmstadt.de or banerjee@chem.tamu.edu.

This article contains supporting information online at http://www.pnas.org/lookup/suppl/doi:10.1073/pnas.2115072119/-/DCSupplemental.

Published January 21, 2022.

and high lithiated phases. Such phase boundaries 1) result in deleterious Li-ion diffusion kinetics (22) and 2) give rise to anisotropic volume changes that engender stress gradients, resulting eventually in fracture, loss of connectivity to the conductive matrix, and capacity fading (22, 24–27). Considerable efforts have been made to suppress phase transformations or to ensure their homogeneity based on control of crystallite size, electrode texture, and substitutional modification (19, 28–31). A distinctive strategy that we explore here involves examining an alternative polymorph that retains the same transition-metal redox reactions but has an entirely different sequence of lithiation-induced structural modifications by dint of its reconfigured atomic connectivity.

We consider here a metastable one-dimensional (1D) tunnel-structured polymorph, ζ-$V_2O_5$, comprising interconnected [$VO_5$] square pyramids and [$VO_6$] octahedra (32). Retaining the chemical composition preserves features of electrochemical performance such as high theoretical capacity and accessibility of redox states as in the thermodynamically stable polymorph (15). From the perspective of kinetics, the substantially different structural motifs of metastable polymorphs define distinctive diffusion pathways (33). Remarkably, our chemical lithiation studies illustrate that the tunnel structure of ζ-$V_2O_5$ is capable of reversibly accommodating up to 1.2 Li-ions (13, 34). Indeed, we have chemically lithiated entire single crystals and mapped pathways traversed by Li-ions across this structure (12). In this study, we contrast the dynamical evolution of lattice structure, electrochemical performance, and electrochemistry–mechanics coupling in metastable ζ-$V_2O_5$ cathodes upon electrochemical cycling and contrast it to electrodes comprising similarly sized particles of its thermodynamically stable counterpart, α-$V_2O_5$ (Fig. 1*A*). We find that ζ-$V_2O_5$ not only exhibits better cycling stability but also exhibits faster Li-ion diffusion. Moreover, the 1D framework of ζ-$V_2O_5$ is preserved upon lithiation/delithiation, whereas the two-dimensional (2D) layered α-$V_2O_5$ structure undergoes irreversible phase transformations. Finally, homogeneous lithiation is observed across ζ-$V_2O_5$ particles without the distinct striping, core–shell motifs, and "hot spots" characteristic of α-$V_2O_5$ (17, 19). As such, the details of atomic connectivity profoundly alter the fundamental mechanisms for accommodating inserted Li-ions and thereby have far-reaching ramifications for cycling stability and rate performance. These results illustrate the promise of using metastable polymorphs to design viable cathodes for next-generation Li-ion batteries (35, 36).

## Results and Discussion

Fig. 1 shows structural and morphological characterization of the as-prepared ζ-$V_2O_5$ and α-$V_2O_5$ nanowires whose synthesis is described in the *Materials and Methods*. ζ-$V_2O_5$ nanowires are prepared from leaching Ag-ions from hydrothermally synthesized β-$Ag_xV_2O_5$ (the two-step preparation is facile, but this polymorph is less synthetically accessible as compared with its thermodynamic counterpart, α-$V_2O_5$, which is readily accessible from direct synthesis and is commercially available at the scale of thousands of tons). Scanning electron microscopy (SEM) observations indicate that both α-$V_2O_5$ and ζ-$V_2O_5$ have a similar nanowire morphology and dimensions. α-$V_2O_5$ nanowires have a rectangular cross-section with lateral dimensions of 183 ± 58 nm; ζ-$V_2O_5$ nanowires have cylindrical cross-sections with the largest lateral dimensions of 106 ± 22 nm. Both α- and ζ-$V_2O_5$ nanowires extend several microns in length, as shown in Fig. 1 *B* and *E*, respectively. *SI Appendix*, Fig. S1 shows transmission electron microscopy (TEM) images. Lattice-resolved high-resolution TEM images as well as selected-area electron diffraction patterns attest to the single-crystalline nature of the nanowires (*SI Appendix*, Fig. S1 *C* and *F*). Fig. 1*C* plots a synchrotron XRD pattern acquired for α-$V_2O_5$ nanowires; Fig. 1*D* shows the crystal structure deduced from a Rietveld refinement to the XRD pattern. The α-$V_2O_5$ nanowires crystallize in an orthorhombic (*Pmmn*) space group with layers of [$VO_5$] square pyramids arrayed in an up–up–down–down configuration (*SI Appendix*, Table S1) (18). In contrast, the XRD pattern acquired for ζ-$V_2O_5$ nanowires plotted in Fig. 1*F* can be indexed to a monoclinic (*C*2/*m*) crystal structure with a 1D tunnel along the crystallographic *b*-axis as depicted in Fig. 1*G* (*SI Appendix*, Table S2) (12, 34). Notably, despite being metastable, ζ-$V_2O_5$ does not readily decompose into α-$V_2O_5$, the thermodynamically stable polymorph. *SI Appendix*, Fig. S2 shows in situ heating powder XRD, illustrating that the transformation of ζ-$V_2O_5$ to α-$V_2O_5$ is initiated only at temperatures >500 °C.

Fig. 2 contrasts the electrochemical performance of α-$V_2O_5$ and ζ-$V_2O_5$ nanowires. For α-$V_2O_5$, the first discharge process shows potential plateaus at 3.39, 3.20, 2.37, and 2.06 V (Fig. 2*A*), which are consistent with pronounced reduction peaks observed by cyclic voltammetry in Fig. 2*B*. The plateaus arise from a sequence of intercalation-induced phase transformations: α → ε, ε → δ, δ → γ, and γ → ω (*SI Appendix*, Fig. S3) (37–39). The potential plateaus observed during the initial discharge cycle disappear during charging as a result of irreversible phase transformations resulting in the formation of γ-$Li_xV_2O_5$ (at $x > 1$). The specific discharge capacity is reduced from 283.0 mAh/g to 233.9 mAh/g and then to 208.7 mAh/g after three cycles (Fig. 2*A*). The electrochemical characteristics of ζ-$V_2O_5$ are markedly different. While several plateaus are observed during discharge (Fig. 2*D*), as we will demonstrate below from *operando* XRD studies, these derive not from distortive changes of the 1D tunnel framework but are instead a result of the reordering of Li-ions within interstitial sites along the tunnels (12, 34). As such, these potential slopes are fully recovered during the charging processes, which, together with retention of the anodic and cathodic waves in the cyclic voltammetry plots shown in Fig. 2*E*, indicates a high degree of reversibility of Li-ion intercalation/deintercalation.

α-$V_2O_5$ and ζ-$V_2O_5$ have further been fashioned into cathodes of coin cells using the same electrode specifications and cycled at a C-rate of C/2 between 2.0 and 4.0 V for 100 cycles, as shown in Fig. 2 *C* and *F*, respectively. Two additional datasets for both α-$V_2O_5$ and ζ-$V_2O_5$ are plotted in *SI Appendix*, Figs. S4 and S5, respectively. Reported capacity values and SDs were calculated based on these triplicate measurements. The initial specific capacity of α-$V_2O_5$ is 285 ± 48 mAh/g but is decreased to 190 ± 28 mAh/g (67 ± 3% of the starting value) after 50 cycles and to only 136 ± 22 mAh/g (48 ± 1% of the initial value) after 100 cycles. The capacity fading directly reflects the irreversible structural distortions in this polymorph. For ζ-$V_2O_5$, the initial capacity is 178 ± 12 mAh/g; 153 ± 21 mAh/g, 86 ± 6% of the initial capacity, is retained after 50 cycles, and 140 ± 6 mAh/g (79 ± 3% of the initial capacity) is retained after 100 cycles. Notably, the electrode specifications have been kept as similar as possible across the two polymorphs to enable comparison of the effects of crystal structure on electrochemical processes. Practical electrode architectures must further enable effective utilization of the active material through incorporation of curvature, optimization of crystallite as well as particle dimensions and morphologies, and appropriate mesoscale structuring of the electrode (19, 40). As such, even without optimization of crystallite geometries, ζ-$V_2O_5$ exhibits vastly improved cycling stability, which can be ascribed to its structure retention during Li-ion intercalation/deintercalation.

Fig. 2*G* presents the rate performance of ζ-$V_2O_5$ ranging from C/20 to 5C for 555 cycles. Remarkably, the initial discharge capacity at 5C is 171 mAh/g, and a capacity of 135.0 mAh/g is retained even after 540 cycles, indicating excellent cycling stability for ultralong cycling. A high capacity of 320 mAh/g is recovered upon reducing the C-rate from 5C to C/20. In stark contrast, *SI Appendix*, Fig. S6 shows that the initial discharge capacity of α-$V_2O_5$ is drastically decreased from 277 mAh/g at C/20

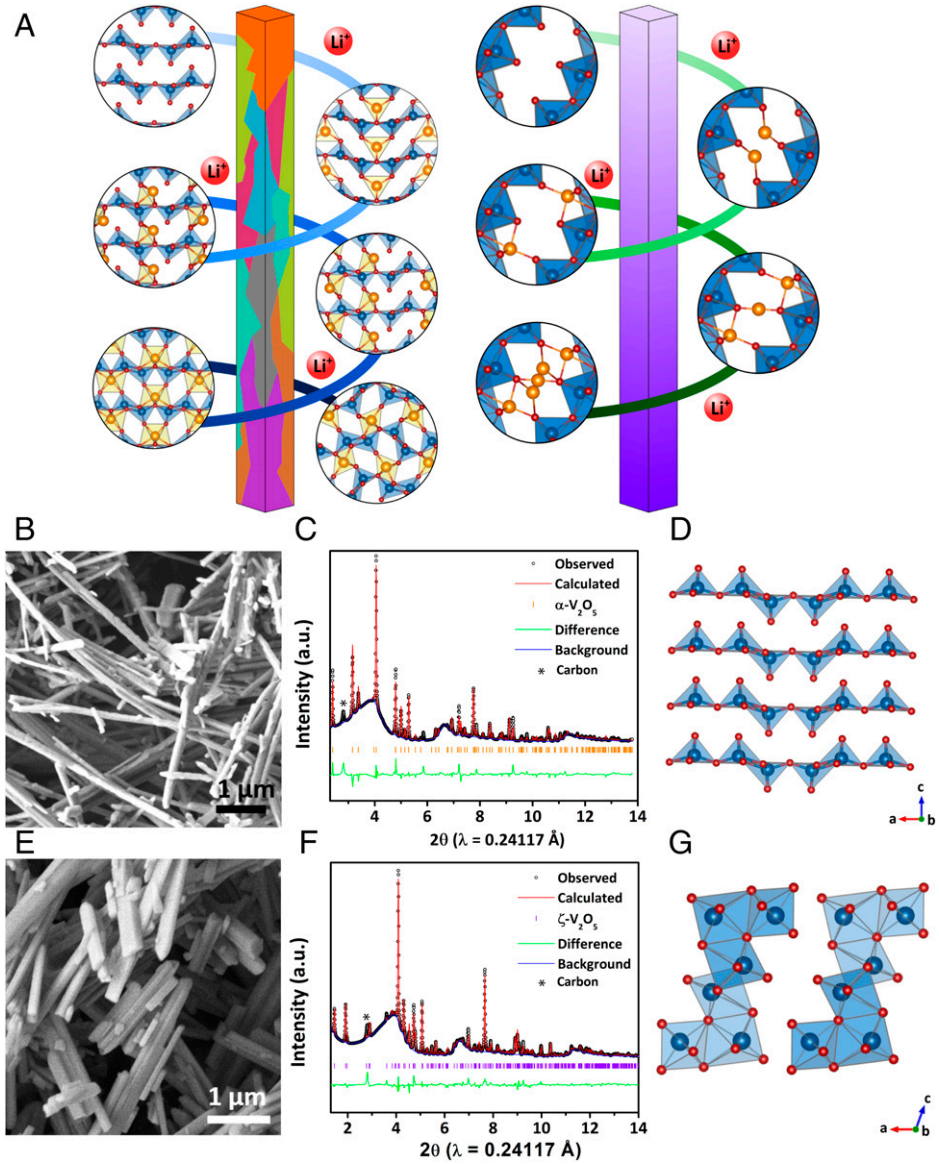


**Fig. 1.** Morphological and structural characterization of α-$V_2O_5$ and ζ-$V_2O_5$. (*A*) Schematic illustration of the lithiation process of α-$V_2O_5$ (*Left*) and ζ-$V_2O_5$ (*Right*) nanowires. Li-ion intercalation induces a sequence of phase transitions in α-$V_2O_5$, resulting in phase heterogeneity within particles and across porous electrodes. In contrast, Li-ion intercalation in ζ-$V_2O_5$ simply induces Li-ion reordering along the 1D tunnels, resulting in completely homogeneous lithiation of ζ-$V_2O_5$ nanowires. (*B* and *E*) SEM images of (*B*) α-$V_2O_5$ and (*E*) ζ-$V_2O_5$ nanowires. (*C* and *F*) High-resolution synchrotron powder XRD data (λ = 0.24117 Å) acquired for (*C*) α-$V_2O_5$ and (*F*) ζ-$V_2O_5$ nanowires. The intensity of a.u. is referred as arbitrary unit. (*D* and *G*) Crystal structures of (*D*) α-$V_2O_5$ and (*G*) ζ-$V_2O_5$ as deduced from Rietveld refinements. A feature in the powder XRD patterns for both refinements at ~2θ = 2.8 has not been modeled and shows up in the difference curve as a prominent feature asterisked in *C* and *F*; this reflection derives from carbon material used to construct the electrochemical cells. The absence of modulation of intensity or position of this feature as a function of electrochemical cycling suggests that it remains unaltered across electrochemical processes. *SI Appendix*, Tables S1 and S2 lists the space group, unit cell parameters, and refinement characteristics .

to 200 mAh/g at C/4, 132 mAh/g at C/1.5, and only 1.3 mAh/g at 5C. Only a discharge capacity of 185 mAh/g is maintained when the C-rate is recovered to C/20 after 555 cycles. As such, ζ-$V_2O_5$ presents not only long life-time cycling stability but also outstanding rate capability.

In order to examine the structural origins of the disparate electrochemical characteristics observed for α- and ζ-$V_2O_5$, *operando* synchrotron XRD studies have been performed, as shown in Fig. 3. During initial discharge to 3.37 V ($x$ in $Li_xV_2O_5$, $0 < x < 0.13$), the layered structure shows a slight expansion of layer spacing, resulting in the formation of α-$Li_xV_2O_5$. In the voltage range between 3.37 and 3.35 V ($x$ in $Li_xV_2O_5$, $0.13 < x < 0.3$), the increasing concentration of Li-ions is accommodated by puckering of the layers and expansion of the interlayer spacing, stabilizing an ε-$Li_xV_2O_5$ phase (*SI Appendix*, Fig. S3); a notable biphasic regime is observed in this potential window with coexistence of α-$Li_xV_2O_5$ and ε-$Li_xV_2O_5$ (see Fig. 5*A*). The layer spacing of ε-$Li_xV_2O_5$ is gradually expanded with increasing Li-ion concentration until discharge to 3.16 V, representing a solid-solution lithiation regime $0.3 < x < 0.88$. With further discharge until 2.35 V ($x$ in $Li_xV_2O_5$, $0.88 < x < 1.07$), the emergence of distorted ε′-$Li_xV_2O_5$ and δ-$Li_xV_2O_5$ phases are observed (*SI Appendix*, Fig. S3) (41). The δ-$Li_xV_2O_5$ phase is derived from ε-$Li_xV_2O_5$ by a pronounced shifting of layers along the *b*-axis (*SI Appendix*, Fig. S3) (42). With still further lithiation down to 2.34 V ($x$ in $Li_xV_2O_5$, $1.07 < x$), a strongly distorted γ-$Li_xV_2O_5$ phase is nucleated; a pronounced phase coexistence regime is observed comprising ε′-$Li_xV_2O_5$, δ-$Li_xV_2O_5$, and

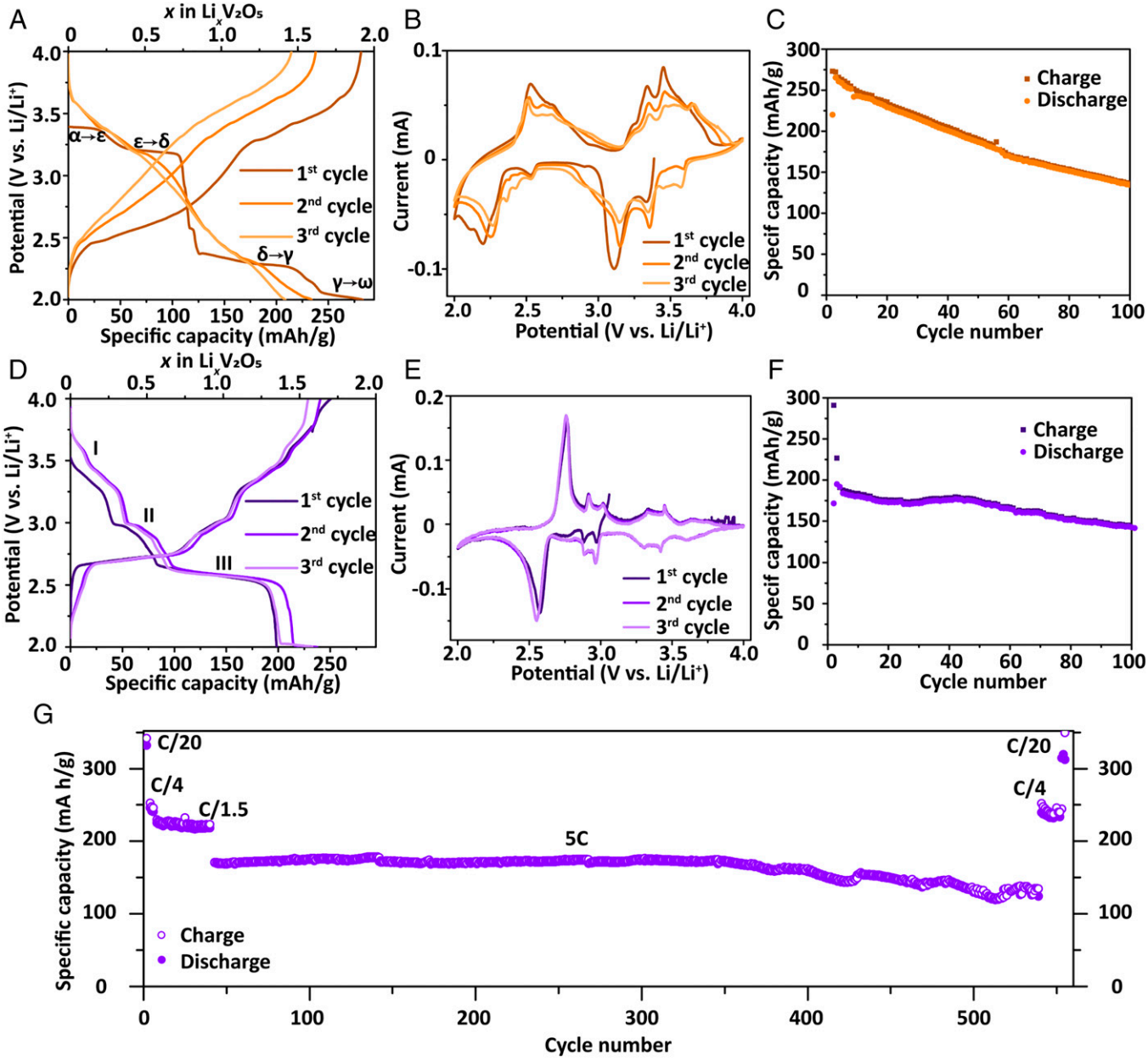


**Fig. 2.** Electrochemical measurements contrasted for $V_2O_5$ polymorphs. (*A* and *D*) Galvanostatic measurements performed for α-$V_2O_5$ (*A*) and ζ-$V_2O_5$ (*D*) cathodes in the range between 2.0 and 4.0 V versus $Li^+$/Li at a C-rate of C/20. (*B* and *E*) Cyclic voltammetry measurements of α-$V_2O_5$ (*B*) and ζ-$V_2O_5$ (*E*) in the range between 2.0 and 4.0 V at a sweep rate of 0.1 mV/s. (*C* and *F*) Cycling performance of α-$V_2O_5$ (*C*) and ζ-$V_2O_5$ (*F*) coin cells between 2.0 and 4.0 V at a C-rate of C/2 for 100 cycles. (*G*) Rate performance of ζ-$V_2O_5$ ranging from C/20 to 5C between 2.0 and 4.0 V.

γ-$Li_xV_2O_5$. Lattice parameters of each phase are noted in *SI Appendix*, Table S3, the corresponding structures are shown in *SI Appendix*, Fig. S3, and a (transient) Li-$V_2O_5$ phase diagram is plotted (see Fig. 5*A*).

During the charging process, a phase mixture of δ-$Li_xV_2O_5$ and γ-$Li_xV_2O_5$ is remnant down to 2.51 V. Upon further delithiation from 2.51 V until 3.21 V, ε′-$Li_xV_2O_5$ is stabilized, coexisting with δ-$Li_xV_2O_5$ and γ-$Li_xV_2O_5$. Upon still further delithiation, a mixture of ε-$Li_xV_2O_5$, δ-$Li_xV_2O_5$, and γ-$Li_xV_2O_5$ is observed before 3.32 V. As such, a primary consequence of the distortive phase transitions in α-$V_2O_5$ is the need for an overpotential to restore the same lithiated/delithiated states upon charging. Fig. 3*B* shows a magnified view of the 2θ range corresponding to 001 and 101 reflections, indicating that intercalation/deintercalation is not fully reversible. Indeed, at the end of a charged state, the irreversible phase of γ-$Li_xV_2O_5$ is observed to persist, yielding a mixture of ε-$Li_xV_2O_5$ and γ-$Li_xV_2O_5$.

Analogous *operando* synchrotron XRD measurements have been performed for ζ-$V_2O_5$ cathodes and are plotted in Fig. 3 *D*–*F*. Fig. 3 *D* and *E* demonstrate the complete reversibility of lithiation/delithiation processes in ζ-$V_2O_5$, which provides a stark contrast to the clear irreversibility evident for α-$V_2O_5$ in Fig. 3 *A*–*C*. In Fig. 3*D*, different lithiation regimes corresponding to slopes in the discharge curve are identified; however, notably across all these regimes, the monoclinic *C*2/*m* space group is retained and the 1D tunnel structure of ζ-$V_2O_5$ is entirely preserved. Instead, the observed features in the discharge curves correspond to reordering of Li-ion occupancies within interstitial sites of the tunnel framework. The specific interstitial sites occupied by Li-ions within the tunnel have been identified from single-crystal XRD

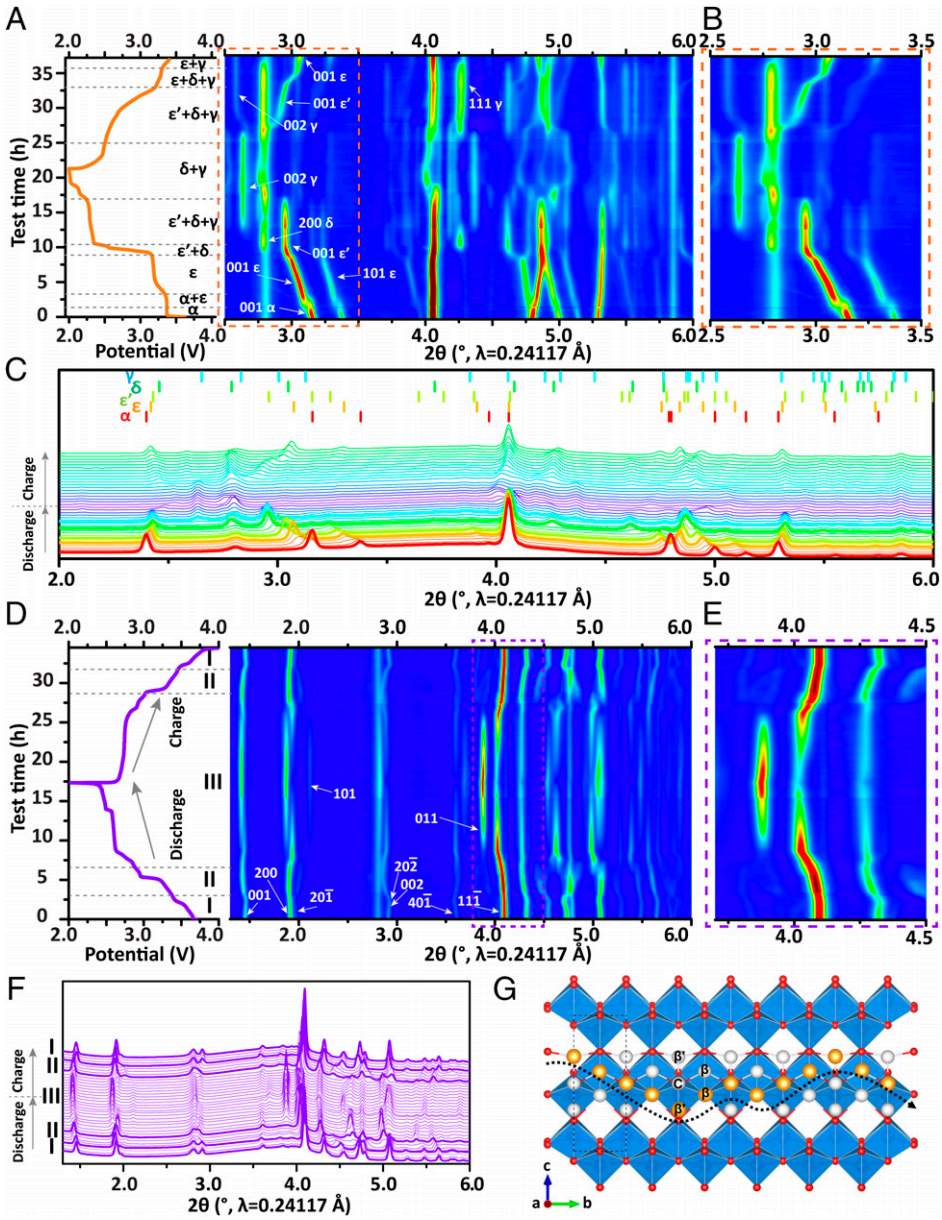


**Fig. 3.** *Operando* XRD data collected using AMPIX cells during electrochemical cycling of α-$V_2O_5$ and ζ-$V_2O_5$. (*A* and *D*) Discharge/charge profile (*Left*) of α-$V_2O_5$ (*A*) and ζ-$V_2O_5$ (*D*) at a C-rate of *C*/20 and contour plot of intensities of corresponding reflections (*Right*). (*B* and *E*) Magnified view of diffraction intensity contour plot of α-$V_2O_5$ (*B*) in the 2θ range from 2.5 to 3.5° as highlighted in *A* and of ζ-$V_2O_5$ (*E*) in the 2θ range from 3.7 to 4.5° as highlighted in *D*. (*C* and *F*) Waterfall plot of select diffraction patterns acquired during lithiation/delithiation of α-$V_2O_5$ (*C*), illustrating intercalation-induced phase transformations and regions of multiphase coexistence, and ζ-$V_2O_5$ (*F*), demonstrating $Li^+$ reordering in the tunnels. In *C*, red ticks denote reflections indexed to α-$Li_xV_2O_5$; orange ticks denote reflections indexed to ε-$Li_xV_2O_5$; green ticks denote reflections indexed to ε′-$Li_xV_2O_5$; light green ticks denote reflections indexed to δ-$Li_xV_2O_5$; and light blue ticks denote reflections indexed to γ-$Li_xV_2O_5$. For α-$V_2O_5$, δ-$Li_xV_2O_5$ is clearly discernible upon further charging all the way to 3.32 V, which is higher than the 3.16 V discharge voltage where the δ-$Li_xV_2O_5$ phase is first observed during lithiation. (*G*) Cutaway view of the ζ-$V_2O_5$ tunnel viewed down the *a*-axis. White spheres indicate possible Li positions (β′, β, and C, respectively) in a highly lithiated structure, with orange spheres used to highlight the positions of an Li-ion along a proposed diffusion pathway down the tunnel *b*-axis (the course of which is indicated with a black dashed arrow) (12).

studies of chemically prepared single crystals of β/β′-$Li_xV_2O_5$ and are depicted in *SI Appendix*, Fig. S7 (12). *Operando* synchrotron XRD studies enable identification of the sequence in which interstitial sites are occupied with increasing depth of discharge. In the initial insertion regime (labeled I, $0 < x < 0.30$ in $Li_xV_2O_5$; Table 1), a slight enlargement of the tunnel is observed upon discharging until 3.38 V and, from comparison with single-crystal XRD studies, indicates the initial filling of β sites within the 1D tunnel of ζ-$V_2O_5$. Upon further discharge to 2.89 V, $0.30 < x < 0.66$, located in Regime II, the coexistence of two distinctive Li-ion occupancies is noted; specifically, both β and β′ sites within the 1D tunnel of ζ-$V_2O_5$ are occupied with increasing concentration of Li-ions, with the more spatially separated β′ sites favored with increasing lithiation. As shown in Table 1, across these two regimes, there is a <2.4% volume expansion of the lattice as compared with unlithiated ζ-$V_2O_5$. At still deeper discharge down to 2.0 V ($0.66 < x < 1.8$) in Regime III, the tunnel framework is still preserved. Greater expansion of the tunnel (~8.9%) is observed in order to accommodate a higher concentration of Li-ions, first filling the β′ and C sites, which are aligned down the center of the tunnel,

**Table 1. Lithium occupancies of various lithiated states and lattice parameters corresponding to each of the insertion regimes for ζ-$V_2O_5$ during electrochemical lithiation as deduced from *operando* synchrotron XRD measurements**

| $x$ in $Li_xV_2O_5$ | Regime | Potential (V) | $a$ (Å) | $b$ (Å) | $c$ (Å) | β (°) | $V$ (Å$^3$) | Space group | Sites occupied (12) | Reversible (Y/N) |
|---|---|---|---|---|---|---|---|---|---|---|
| 0 | Unlithiated | 3.65 | 15.311 | 3.606 | 10.093 | 109.857 | 524.167 | *C2/m* | N/A | Y |
| $0 < x \leq 0.3$ | I | 3.65–3.38 | 15.377 | 3.606 | 10.076 | 110.115 | 524.685 | *C2/m* | β | Y |
| $0.3 < x \leq 0.66$ | II | 3.38–2.89 | 15.287 | 3.629 | 10.131 | 109.011 | 531.413 | *C2/m* | β′ | Y |
| | | | 15.302 | 3.621 | 10.162 | 107.553 | 536.893 | *C2/m* | | Y |
| $0.66 < x \leq 1.8$ | III | 2.89–2.0 | 15.327 | 3.671 | 10.278 | 111.423 | 538.294 | *C2/m* | β′ + C | Y |
| | | | 16.338 | 3.882 | 9.953 | 115.317 | 570.659 | *C2/m* | β′ + C + β | Y |

*Operando* synchrotron XRD measurements related in Fig. 3 *D–F*. N/A, not applicable.

followed by significant expansion of the structure along the *b*-axis in order to allow for filling of the β′, C, and β sites simultaneously, as shown in *SI Appendix*, Fig. S7 (12). An inferred Li-ion diffusion pathway along the 1D tunnel of ζ-$V_2O_5$ is shown in Fig. 3*G* (12). By comparison, the volume change for δ-$Li_xV_2O_5$ ($0.88 < x$) as compared with $V_2O_5$ is 11.8%.

During the charging process, this highly lithiated regime is delithiated in steady succession to stabilize Regimes III, II, and I before finally recovering the empty tunnel structure of ζ-$V_2O_5$ at the end of the charge cycle (Fig. 3*E*). As such, the Li-ion occupancies in interstitial tunnel sites are modified in response to increasing/decreasing Li-ion concentration without substantial bond-breaking/bond-making and displacive phase transitions of the $V_2O_5$ framework. The pronounced voltage hysteresis between discharge and charge cycles in α-$V_2O_5$ derived from structural transformations is notably absent here. The excellent structural reversibility and preservation of the 1D tunnel framework underpins the reversibility and substantially higher capacity retention observed in Fig. 2.

Further evaluation of phase heterogeneities but at the level of individual particles has been performed using STXM, a synchrotron-based X-ray spectromicroscopy technique (43, 44). Ex situ STXM hyperspectral maps acquired for lithiated α- and ζ-$V_2O_5$ nanowires shown in Fig. 4 correspond to V $L_3$-, V $L_2$-, and O K-edge X-ray absorption near-edge structure (XANES) spectra acquired at each pixel. The fine structure features at the V $L_3$-edge and O K-edge evolve with increasing lithiation as a result of modifications to the electronic and atomistic structure resulting from concomitant reduction of vanadium centers and lattice distortions to accommodate the inserted ions (19, 23, 29, 45). V $L_3$-edge XANES spectra correspond to transitions from $V2p_{3/2} \rightarrow V_{3d}$-derived states; upon lithiation and concomitant reduction of vanadium centers, the intensities of the fine features corresponding to $V_{3d}$ states at the conduction band edge are diminished as electrons fill previously unoccupied states (Pauli darkening). In turn, O K-edge XANES spectra correspond to transitions from O 1s core levels to O 2p states hybridized with V 3d states. Lithiation brings about a pronounced modification of the relative intensities of $t_{2g}$ and $e_g$* features as a result of 1) lattice distortions resulting from Li–O interactions that remove degeneracy of spin-up and spin-down states and 2) emergence of electron correlation effects (10, 19, 23, 29, 46). As such, STXM serves as a sensitive probe for mapping electron localization and, by proxy, the extent of lithiation (10, 19, 23, 29, 46).

Fig. 4*A* shows an STXM optical-density map collected for an ensemble of chemically lithiated α-$V_2O_5$ nanoparticles. In STXM, incident X-rays ($I_0$) are attenuated as per $I = I_0\exp(\mu t)$, where μ is a linear absorption coefficient that is composition and energy dependent and $t$ corresponds to material thickness. Region of interest (ROI) analyses of the hyperspectral data are presented in Fig. 4 *B* and *C* and reveal significant heterogeneity across the particles despite identical lithiation conditions. Three ROIs have been distinguished by orange, blue, and yellow colored infills in Fig. 4*B*. The corresponding spectral profiles across V L-edge and O K-edge are plotted in Fig. 4*C* and are arranged in order of increasing lithiation (*Bottom* to *Top*) based on comparison with previously reported standards and first-principles density functional theory simulations; varying extents of lithiation are characterized by changes in relative intensity and peak positions of V $L_3$- and O K-edge features (19, 29). Fig. 4*D* shows considerable phase heterogeneity (and phase coexistence) in an ensemble of α-$V_2O_5$ nanowires. O K-edge spectra shown in Fig. 4*E* provide further evidence of lithiation heterogeneity observed as a pronounced diminution in the intensity of the $t_{2g}$ feature relative to $e_g$* in going from Region 1 to Region 3 (10, 19, 23, 29, 46). Fig. 4 *F–J* shows the same ROI analysis performed for an ensemble of electrochemically lithiated ζ-$V_2O_5$ particles. The STXM optical-density map is shown in Fig. 4*F*, ROIs have been spatially defined in Fig. 4*G*, the corresponding XANES spectra are plotted in Fig. 4*H*, and expanded views of the V $L_3$-edge and O K-edge across the ROIs are provided in Fig. 4 I and J, respectively. For the ROIs shown in Fig. 4*G*, only subtle differences in spectral sharpness are observed across the V L-edge and O K-edge, which can be attributed to thickness variations (see the thickness profiles for each ROI in *SI Appendix*, Fig. S8) (19). The absence of any discernible lithiation heterogeneities present across ensembles of ζ-$V_2O_5$ nanowires reflects the more facile cation reordering mechanism for accommodating Li-ions. The ROIs shown in Fig. 4 *F–J* have been interpreted using XANES data acquired for chemically lithiated standards (13) and reveal little to no heterogeneity between the selected regions aside from some minor variations of intensity profiles attributable to particle thickness. As such, STXM imaging of ensembles of lithiated α-$V_2O_5$ nanowires illustrate considerable phase coexistence, reflecting the accommodation of Li-ions through phase transformations. In contrast, no discernible lithiation heterogeneities are observed across ensembles of ζ-$V_2O_5$ nanowires, reflecting the more facile cation reordering mechanism for accommodating Li-ions.

Fig. 5 *A* and *B* plot the transient Li-$V_2O_5$ phase diagram of α-$V_2O_5$ and an equivalent depiction of monophasic cation reordering in ζ-$V_2O_5$ as deduced from *operando* synchrotron XRD measurements. These panels illustrate the stark differences in lithiation mechanisms across the two polymorphs. In order to connect these disparate lithiation mechanisms to the pronounced differences in electrochemical performance and capacity retention observed in Fig. 2, we have further performed galvanostatic intermittent titration technique (GITT) measurements to evaluate diffusion coefficients and *operando* multibeam optical stress sensor (MOSS) measurements to examine electrochemistry–mechanics coupling.

The Li-ion diffusion coefficients of α-$V_2O_5$ vary nonuniformly across four orders of magnitude from $10^{-10}$ to $10^{-14}$ $cm^2 \cdot s^{-1}$ as a function of the extent of lithiation (*SI Appendix*, Fig. S9*A*) (22). The highest values of $D_{Li}$ are observed in the voltage range corresponding to a monophasic region of the phase diagram (22). Notably, ζ-$V_2O_5$ shows $D_{Li}$ values ranging from $1 \times 10^{-12}$ to $3 \times 10^{-9}$ $cm^2 \cdot s^{-1}$ (*SI Appendix*, Fig. S9*B*). With initial lithiation, $D_{Li}$ gradually decreases from $3 \times 10^{-9}$ to $5 \times 10^{-10}$ $cm^2 \cdot s^{-1}$, corresponding to increased fractional occupation of β sites. With

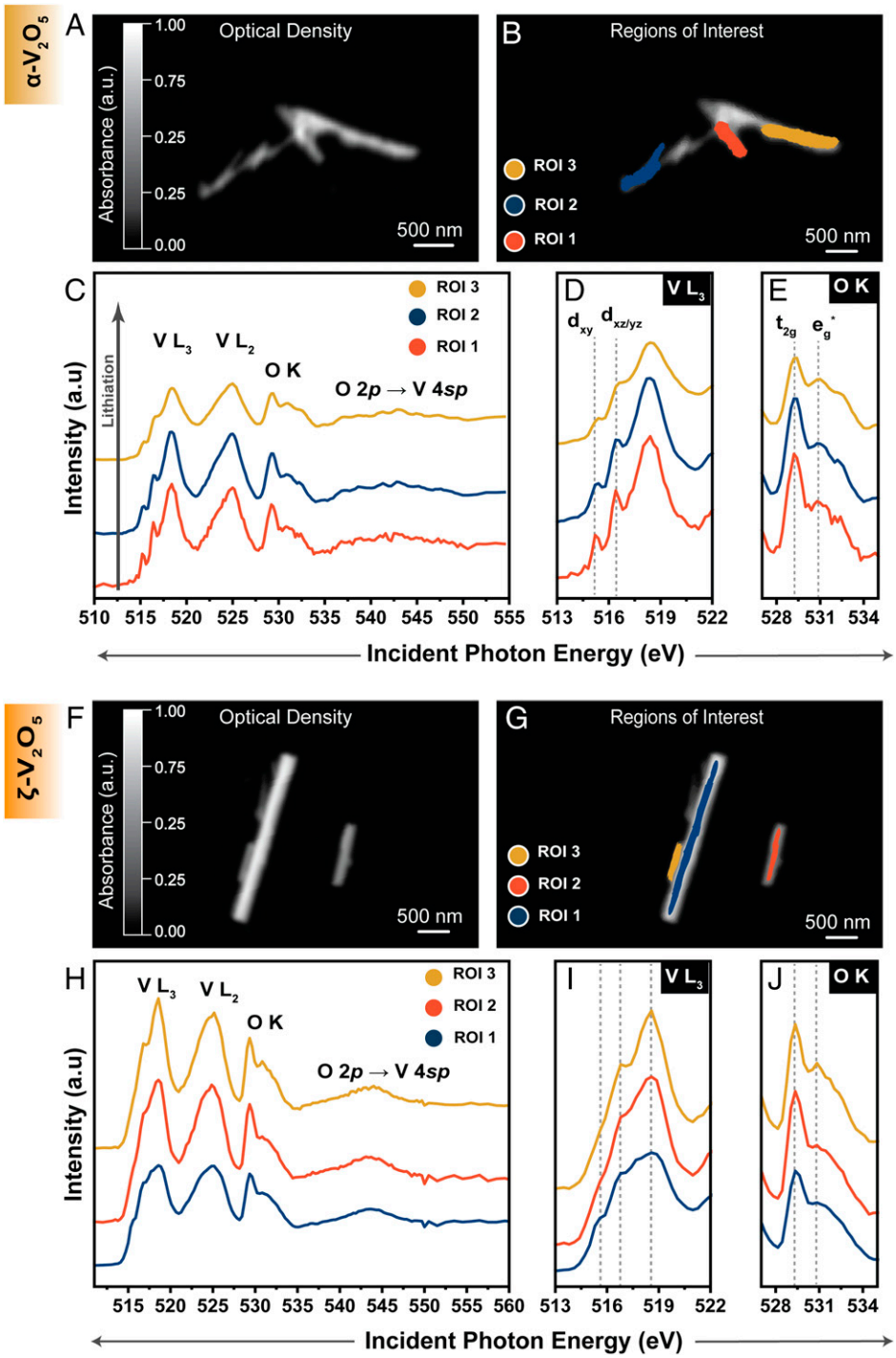


**Fig. 4.** Lithiation heterogeneities (and lack thereof) in α-$V_2O_5$ and ζ-$V_2O_5$ nanowires as imaged using STXM. (*A* and *F*) STXM optical-density images collected for a network of α-$V_2O_5$ (*A*) and ζ-$V_2O_5$ nanowires (*F*); (*B* and *G*) ROIs defined across the imaged sample differentiated using orange, blue, and yellow markers; X-ray absorption near-edge spectra corresponding to the ROIs are shown in *C* to *E* for α-$V_2O_5$ and *H* to *J* for ζ-$V_2O_5$. (*C* and *H*) Integrated spectrum obtained by averaging the spectrum of each pixel contained within ROIs 1 to 3 demarcated for α-$V_2O_5$ (*C*) and ζ-$V_2O_5$ (*H*). The spectra are arranged in order of increasing lithiation (*Bottom* to *Top*). Magnified views of the V $L_3$-edge (*D* and *I*) and O K-edge (*E* and *J*) are presented across the ROI.

further discharge to 3.0 V, $D_{Li}$ is slightly increased and maintained at $\sim 1 \times 10^{-9}$ $cm^2 \cdot s^{-1}$ as the full complement of β′ sites are occupied, and cation reordering opens up β sites, enhancing Li-ion mobility. Upon lithiation down to 2.0 V ($1.0 < x$), $D_{Li}$ is decreased to $1 \times 10^{-12}$ to $5 \times 10^{-11}$ $cm^2 \cdot s^{-1}$ as the tunnel is fully occupied (Table 1). The cation reordering mechanism operational in this polymorph thus ensures a relatively high $D_{Li}$ value by mitigating the formation of phase boundaries. The diminution of Li-ion diffusivity at high depths of discharge due to filling of the tunnel may be partially resolved by the significantly expanded lattice allowing for diffusion between tunnels. This allows for the excellent high-rate performance evidenced in Fig. 2*G*. While ζ-$V_2O_5$ shows substantially improved reversibility, overpotential, ionic conductivity, and capacity retention as compared with α-$V_2O_5$, it does have a greater propensity for self-discharge than ζ-$V_2O_5$. *SI Appendix*, Fig. S10 plots the change in open circuit

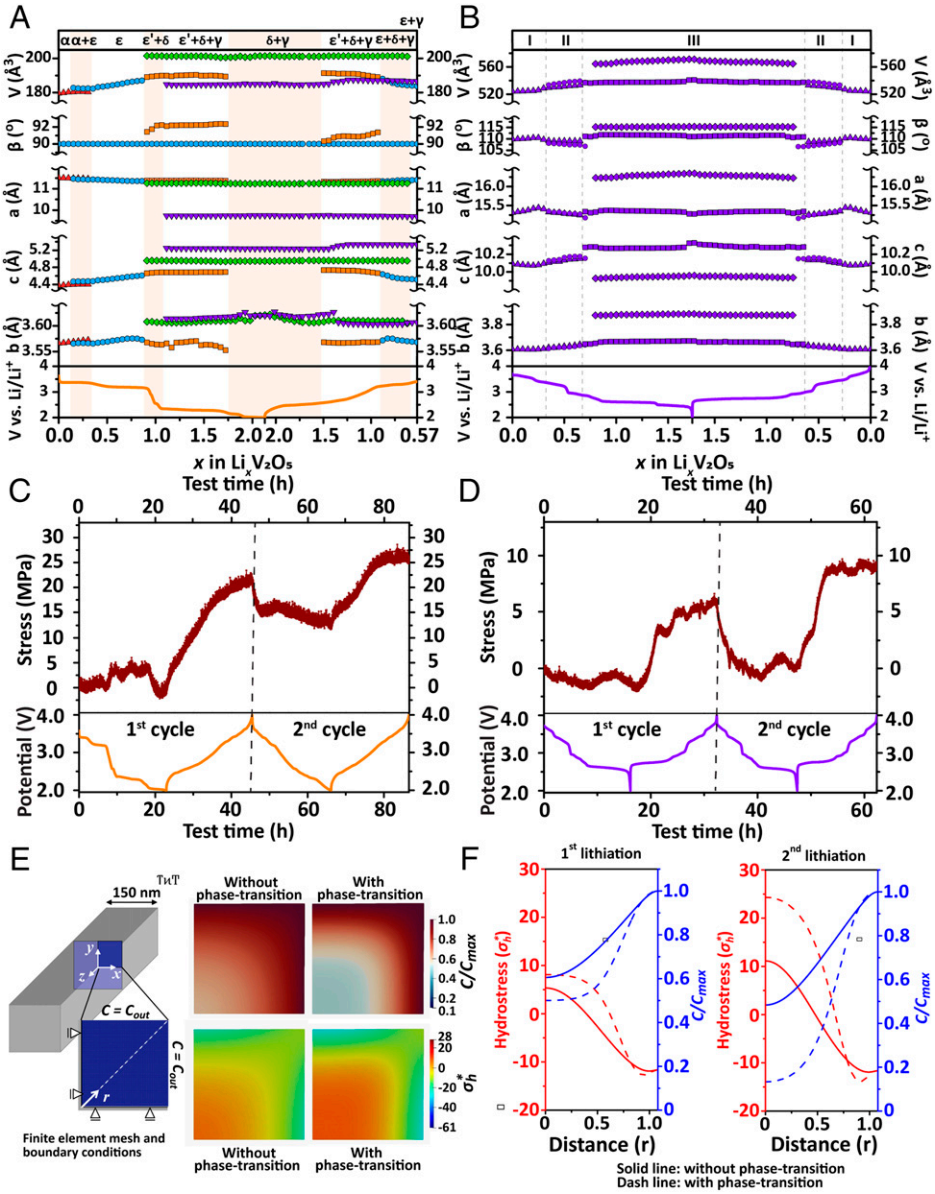


**Fig. 5.** Phase depictions, mechanical measurement, and mechanical simulations of α-$V_2O_5$ and ζ-$V_2O_5$. (*A*) Transient Li-$V_2O_5$ phase diagram (*Top*) of α-$V_2O_5$ deducted from *operando* synchrotron XRD (Fig. 3) performed concurrently with galvanostatic measurements (*Bottom*) at a C-rate of C/20. To enable a direct comparison of layer spacing changes, *c*-axis values and volumes of δ-$Li_xV_2O_5$ and γ-$Li_xV_2O_5$ are divided in half (the unit cell is doubled for these structures as compared with α-$Li_xV_2O_5$, and ε/ε′-$Li_xV_2O_5$). (*B*) Li-$V_2O_5$ phase depiction (*Top*) of monophasic cation reordering in ζ-$V_2O_5$ as deduced from *operando* synchrotron XRD measurements (*Bottom*) of ζ-$V_2O_5$ at a C-rate of C/20. (*C* and *D*) Stress variation (*Top*) measured with MOSS during galvanostatic cycling (*Bottom*) at a C-rate of C/20 between 2.0 and 4.0 V for α-$V_2O_5$ (*C*) and ζ-$V_2O_5$ (*D*). (*E*) Simplified 2D geometry and boundary conditions for numerical studies of $V_2O_5$ nanowires (*Left*); lithium concentration and normalized hydrostatic stress distribution obtained from phase-field simulations for $V_2O_5$ nanowires with (α-$V_2O_5$) and without (ζ-$V_2O_5$) phase transitions (*Right*). (*F*) Distribution of lithium concentration and normalized hydrostatic stress inside of electrode along with the radial axis for the first (*Left*) and second lithiation (*Right*) cycles.

voltage as a function of time for two cells of each of the two polymorphs, suggesting relatively greater self-discharge for ζ-$V_2O_5$.

The coupling between electrochemistry and mechanics is of pivotal importance to Li-ion diffusion and capacity retention in electrode materials (26, 47–49). The fundamentally distinctive mechanisms of lithiation in α- and ζ-$V_2O_5$ are expected to give rise to significantly different stress accumulation upon electrochemical cycling (50). Table 1 and *SI Appendix*, Table S3 delineate the substantial differences in lithiation-induced volume expansion between the two phases. *Operando* MOSS measurements have been performed during electrochemical cycling, and the extrapolated stress response is plotted in Fig. 5 *C* and *D* for α-$V_2O_5$ and ζ-$V_2O_5$, respectively. Fig. 5 *C* and *D* show the measured in-plane stress profiles for working electrodes constructed from the two polymorphs. The in-plane stresses developed as a result of lithiation/delithiation are inferred by measuring the curvature of the substrate as shown in *SI Appendix*, Fig. S11. Stress accumulation relative to the starting state is 25.8 MPa for α-$V_2O_5$ and 9.0 MPa for ζ-$V_2O_5$ after two cycles. As indicated in Figs. 2*A* and 3 *A*–*C*, α-$V_2O_5$ displayed extended phase irreversibility during first electrochemical cycling. As such, we find accumulation of tensile stresses at the end of the first cycle for α-$V_2O_5$ as shown in Fig. 5*C*. In contrast, the electrochemical cycling performance of ζ-$V_2O_5$ appears to be structurally reversible, as shown in Figs. 2*D* and 3 *D*–*F*. ζ-$V_2O_5$ shows considerably less stress accumulation as compared

with α-$V_2O_5$. Notably, some residual stress can be attributed to formation of the cathode electrolyte interface (50, 51).

In order to understand how the distinctive phase transition and cation reordering mechanisms in α- and ζ-$V_2O_5$ affect lithiation heterogeneities and stress accumulation, a phase-field model has been implemented for mechanically coupled Cahn-Hilliard–type diffusion to examine the spatiotemporal distribution of Li-ions in α- and ζ-$V_2O_5$ (Fig. 5 *E* and *F*). Model details can be found in the *SI Appendix*. The finite element calculations are performed based on a 2D plane strain assumption for the cross-section of a sample nanowire system. The details of the geometry, discretization, and boundary conditions are shown in Fig. 5*E*, which depicts the distribution of the Li concentration as well as the normalized hydrostatic stress at the cross-section during the first cycle of lithiation. A higher extent of heterogeneity for both concentration and hydrostatic stress is observed as a result of phase transitions in α-$V_2O_5$ as compared with the cation reordering without phase transition observed in ζ-$V_2O_5$, as observed in the profiled plotted along the radial axis in Fig. 5*F*. During first- and second-cycle lithiation, concentration and normalized stress profiles arising from the phase transition scenario in α-$V_2O_5$ show significant greater magnitudes along the diffusion length. Notably, hydrostatic stress differentials across *r* increase slightly from 17.0 to 22.8 for ζ-$V_2O_5$, whereas this increase is much greater, from 19.8 to 39, for α-$V_2O_5$ characterized by a phase transition. The reduced lithiation heterogeneity and stress accumulation observed for ζ-$V_2O_5$ reflect its distinctive lithiation mechanism (Figs. 3 and 5 *A* and *B*) and reduced volume expansion as compared with the phase transitions characteristic of α-$V_2O_5$; the lower stress accumulation makes ζ-$V_2O_5$ cathodes less prone to fracture and loss of electrochemically active material, thereby contributing to the improved cycling stability observed in Fig. 2.

## Conclusions

In summary, we have examined insertion electrodes of the same composition prepared according to the same electrode specifications and comprising particles with similar dimensions and geometries that differ only in terms of their atomic connectivity and crystal structure, specifically 2D layered α-$V_2O_5$ that crystallizes in an orthorhombic space group and 1D tunnel-structured ζ-$V_2O_5$ crystallized in a monoclinic space group. We find significant differences in voltage hysteresis and capacity retention that are traceable to the distinctive lithiation mechanisms operational in the two polymorphs. *Operando* synchrotron XRD studies performed concurrent with electrochemical cycling allows for examination of the dynamical evolution of structure as a function of Li-ion concentration. A series of intercalation-induced phase transformations, ultimately irreversible beyond $x > 1$ in $Li_xV_2O_5$, is observed for α-$V_2O_5$. In contrast, in ζ-$V_2O_5$ lithiation/delithiation proceeds through reordering of cation occupancies in interstitial sites with complete preservation of the tunnel framework. Ex situ STXM imaging of ensembles of lithiated particles coupled with phase-field modeling confirm the significant phase heterogeneities in α-$V_2O_5$ and homogeneous lithiation of ζ-$V_2O_5$.

The distinct lithiation mechanisms underpinned by differences in crystal structure have profound consequences for electrochemical performance. ζ-$V_2O_5$ exhibits substantially lower stress accumulation as compared with α-$V_2O_5$ in *operando* MOSS experiments and phase-field modeling. By dint of mitigating displacive phase transformations and alleviating large stress gradients, ζ-$V_2O_5$ shows 79 ± 3% capacity retention as compared with 48 ± 1% capacity retention for α-$V_2O_5$ after 100 cycles. Furthermore, ζ-$V_2O_5$ exhibits excellent rate capability, demonstrating that a high capacity of 320 mAh/g is recovered upon cycling with the C-rate ranging from 5C to C/20 after 555 cycles.

The distinctly different lithiation mechanisms observed here are attributable directly to the rigid 1D structure of the metastable ζ-$V_2O_5$ phase as compared with the layered 2D structure of the thermodynamically stable α-$V_2O_5$ phase. In α-$V_2O_5$, a split-off conduction band derived from V $3d_{xy}$ states (arising from crystal field splitting of 3d orbitals in a square pyramidal environment) results in the formation of small polarons, whereas a relatively large change in Li-ion coordination environment ($8 \rightarrow 3 \rightarrow 8$) and a narrow trigonal planar coordination environment of the transition state hinder ion diffusion (52, 53). In contrast, in ζ-$V_2O_5$, considerable overlap of 3d states results in reduced electron masses and lower energy barriers for polaron diffusion (13, 54). The Li-ion diffusion pathway further requires smaller changes in coordination environment, with a $5 \rightarrow 4 \rightarrow 2 \rightarrow 4 \rightarrow 5$ pathway with lower activation energy barriers as sketched in Fig. 3*G* (12).

In summary, this article evidences improved electrochemical performance of ζ-$V_2O_5$, including good capacity retention, excellent rate capability and enhanced Li-ion diffusivity, and reduced stress accumulation. Barriers to Li-ion as well as polaron diffusion are substantially diminished for metastable ζ-$V_2O_5$ in comparison with the thermodynamically stable α-$V_2O_5$ phase (55). The absence of distortive phase transitions facilitates uniform diffusivities across a large voltage window for the metastable ζ-$V_2O_5$ polymorph (albeit with increased self-discharge). The improvement in fundamental material properties is directly relevant to mitigating degradation and safety concerns. Expansion of the 1D tunnel through substitutional doping, optimization of particle geometries (31), and design of mesoscale architectures that enable more effective utilization of the active material (19, 40) further represent promising strategies for designing electrode architectures that realize the full promise of the desirable material properties and intercalation phase diagrams accessible in ζ-$V_2O_5$. The results demonstrate the potential for accessing fundamentally different lithiation mechanisms through reconfiguration of atomic connectivity in metastable polymorphs.

## Materials and Methods

**Material Synthesis.** Both α-$V_2O_5$ and ζ-$V_2O_5$ nanowires were prepared by hydrothermal methods from bulk $V_2O_5$ (≥99.6% trace metals basis; Sigma-Aldrich) as described in previous work (22, 34). Briefly, to prepare α-$V_2O_5$ nanowires, 1.634 g bulk $V_2O_5$ powder and 0.465 g oxalic acid were dispersed in 75 mL deionized water (ρ = 18.2 MΩ/cm). Next, the dispersion was transferred into a 100-mL polytetrafluoroethylene (PTFE) vessel, which was placed within a stainless-steel autoclave. The autoclave was heated at 210 °C for 72 h. After cooling of the vessels under ambient conditions, the obtained precipitate was washed with copious amounts of water and 2-propanol and dried under ambient conditions. The obtained hydrated $V_3O_7$ precipitate was dark green in color. Next, the precipitate was annealed at 450 °C for 24 h in a muffle furnace under a static air atmosphere.

In order to prepare ζ-$V_2O_5$ nanowires, 0.995 g bulk $V_2O_5$ powder and 0.305 g silver acetate were dispersed in 83 mL deionized water (ρ = 18.2 MΩ/cm). Next, the dispersion was placed within a PTFE vessel, which was placed within an autoclave as described above. The autoclave was heated for 5 d at 210 °C and then cooled to room temperature. The obtained β-$Ag_{0.33}V_2O_5$ product was washed with copious amounts of water and 2-propanol (13). Subsequently, 0.300 g $Ag_{0.33}V_2O_5$ was dispersed in 15 mL deionized water and 0.75 to 0.85 mL of HCl (12 M) was added to the dispersion. This mixture was transferred into a 23-mL PTFE vessel for hydrothermal reaction at 210 °C for 24 h. The AgCl precipitate was dissolved by reaction with a 10 wt% aqueous solution of sodium thiosulfate, followed by washing with copious amounts of deionized water (13).

**Materials Characterization.** The particle morphologies of α-$V_2O_5$ and ξ-$V_2O_5$ nanowires were examined by SEM using a JEOL JSM-7500F instrument operating at an accelerating voltage of 5 kV. TEM images, along with selected-area electron diffraction patterns, were acquired using an FEI Tecnai G2 F20 ST instrument operated at an accelerating voltage of 200 kV. TEM samples were prepared by dispersing into 2-proponal, then drop casting onto 400-mesh grids with holey-carbon films supported by copper (Electron Microscopy Science). In situ heating XRD was performed with a Bruker

D8-Vario diffractometer with a Lynxeye detector and MTC oven. The powder sample was mounted on a ceramic heating stage under an $N_2$ atmosphere. Data were collected from 5 to 70° 2θ with a step size of 0.014° and a dwell time of 2 s for ∼1 h scans, with 1-h delays to allow sample equilibration at each temperature. In situ heating XRD measurements of ζ-$V_2O_5$ were performed from 30 to 600 °C.

**Coin Cell Assembly and Electrochemical Measurements.** Coin cells (CR2032) were assembled in an argon-filled glovebox ($H_2O$, $O_2 < 0.1$ ppm). Cathodes comprised 70 wt% (α/ζ) $V_2O_5$ nanowires, 20 wt% SUPER C45 conductive carbon black (MTI Corporation), and 10 wt% poly(vinylidene fluoride) binder (MTI Corporation). Details of electrode preparation are provided in the *SI Appendix*.

Galvanostatic tests and GITT measurements were performed using a LAND battery test system (Wuhan Land Electronics Corporation). Galvanostatic measurements were operated between 2.0 and 4.0 V at C-rates of C/20 and C/2. Cyclic voltammetry measurements were performed using a Biologic potentiostat between 2.0 and 4.0 V at a scan rate of 0.1 mV/s.

The rate capability measurement was carried out by Dimen Inc. The coin cells were charged and discharged under constant current between 2.0 and 4.0 V at various C-rates ranging from approximately C/20 to 5C. GITT measurement is described in the *SI Appendix*.

***Operando* Synchrotron XRD Measurements.** *Operando* XRD measurements were performed using Argonne's multi-purpose in situ X-ray (AMPIX) cells (56), which were assembled within an Ar-filled glovebox ($O_2$, $H_2O < 0.5$ ppm). Cathodes were prepared by compressing pellets (with a diameter of 9 mm) comprising α-$V_2O_5$/ζ-$V_2O_5$ nanowires (70 wt%), PTFE (15 wt%; Sigma-Aldrich), graphite (7.5 wt%), and Vulcan XC-72R carbon (7.5 wt%). Li metal foils were used as anodes (Sigma-Aldrich). The separator was glass fiber (Whatman). The electrolyte was 1 M $LiPF_6$ in a 1:1 (v/v) mixture of ethylene carbonate/diethyl carbonate.

High-resolution synchrotron XRD patterns were collected at beamline 17-BM of the Advanced Photon Source with a wavelength of 0.24117 Å. Image calibration, image integration, Rietveld refinements, and Pawley refinements were performed using GSAS-II (57).

**Mechanical Testing Concurrent with Electrochemical Measurements.** An MOSS from k-Space Associates was used to monitor the curvature of the substrate (Δ*K*) during electrochemical cycling (*SI Appendix*, Fig. S11) (58). Further details are provided in the *SI Appendix*.

**Scanning Transmission X-ray Microscopy.** Briefly, α-$V_2O_5$ nanowires were drop-cast onto a silicon nitride X-ray grid (Norcada) after ultrasonication in 2-propanol. On-substrate lithiation was achieved by direct reaction with a molar excess of *n*-butyllithium (0.01 M) in heptane within an Ar-filled glovebox environment as per

$$V_2O_5(s) + xC_4H_9Li(n-\text{heptane}) \rightarrow Li_xV_2O_5(s) + \frac{x}{2}C_8H_{18}(l)\ldots \quad [1]$$

ζ-$V_2O_5$ nanowires were collected from coin cells discharged to specific voltages. After discharge to desired voltages, the coin cells were disassembled, and the electrodes were washed with copious of dimethyl carbonate. The electrodes were subsequently dried overnight in an Ar-filled glovebox ($H_2O$, $O_2 < 0.1$ ppm). Prior to the STXM measurements, a portion of the active electrode material was ultrasonicated in 2-propanol to create a dispersion from which nanowires could be transferred to an X-ray–transparent silicon nitride grid (Norcada) using drop casting. Lithiated nanowires (both ζ- and α-$V_2O_5$) were washed with anhydrous heptane to remove excess unreacted *n*-butyllithium or electrolyte to prevent the formation of undesirable surficial $Li_xO_y$ species. The grids were sealed under vacuum for transport to the Canadian Light Source for STXM measurements.

STXM measurements were collected at the spectromicroscopy beamline 10D-1 of the Canadian Light Source in Saskatoon, SK, utilizing a 7-mm generalized Apple II elliptically polarizing undulator source. X-ray absorption spectra were acquired across the V $L_2$-, V $L_3$-, and O K-edge elemental absorption edges at each pixel by scanning the incident X-ray energy in the range 510 to 560 eV. The image stack was aligned using a cross-correlation method contained within the aXis2000 software suite. Spectra were pre- and postedge normalized using the Athena software suite to facilitate comparison.

**Phase-Field Model.** Details can be found in the *SI Appendix*.

**Data Availability.** All study data are included in the article and/or *SI Appendix*.

**ACKNOWLEDGMENTS.** This article is based on work supported by Award No. A-1978-20190330 from the Welch Foundation and by Dimien Inc. under NSF Small Business Technology Transfer Grant No. 1938515 and New York State Energy and Research Development Authority Program Opportunity Notice No. 3585. D.S. acknowledges support from an NSF Graduate Research Fellowship under Grant No. 1746932. B.-X.X. acknowledges the German Science Foundation for funding under Project No. 398072825. M. Pharr acknowledges support from the NSF under Award No. DMR-1944674. The authors acknowledge use of the Advanced Photon Source at the 17-BM beamline of Argonne National Laboratory, which was supported by the U.S. Department of Energy, Office of Science, Office of Basic Energy Sciences. A portion of the research described in this article was performed at the Canadian Light Source (SM beamline, 10ID-1).

1. G. Zubi, R. Dufo-López, M. Carvalho, G. Pasaoglu, The lithium-ion battery: State of the art and future perspectives. *Renew. Sustain. Energy Rev.* **89**, 292–308 (2018).
2. J. B. Goodenough, Rechargeable batteries: Challenges old and new. *J. Solid State Electrochem.* **16**, 2019–2029 (2012).
3. J. M. Tarascon, M. Armand, Issues and challenges facing rechargeable lithium batteries. *Nature* **414**, 359–367 (2001).
4. V. Etacheri, R. Marom, R. Elazari, G. Salitra, D. Aurbach, Challenges in the development of advanced Li-ion batteries: A review. *Energy Environ. Sci.* **4**, 3243–3262 (2011).
5. A. Manthiram, An outlook on lithium ion battery technology. *ACS Cent. Sci.* **3**, 1063–1069 (2017).
6. M. S. Whittingham, Lithium batteries: 50 years of advances to address the next 20 years of climate issues. *Nano Lett.* **20**, 8435–8437 (2020).
7. M. S. Whittingham, C. Siu, J. Ding, Can multielectron intercalation reactions be the basis of next generation batteries? *Acc. Chem. Res.* **51**, 258–264 (2018).
8. E. M. Ryan, P. P. Mukherjee, Mesoscale modeling in electrochemical devices—A critical perspective. *Prog. Energy Combust. Sci.* **71**, 118–142 (2019).
9. X. Zhang *et al.*, Multiscale understanding and architecture design of high energy/power lithium-ion battery electrodes. *Adv. Energy Mater.* **11**, 2000808 (2021).
10. L. R. De Jesus, J. L. Andrews, A. Parija, S. Banerjee, Defining diffusion pathways in intercalation cathode materials: Some lessons from $V_2O_5$ on directing cation traffic. *ACS Energy Lett.* **3**, 915–931 (2018).
11. P. M. Marley *et al.*, Emptying and filling a tunnel bronze. *Chem. Sci. (Camb.)* **6**, 1712–1718 (2015).
12. J. V. Handy, Y. Luo, J. L. Andrews, N. Bhuvanesh, S. Banerjee, An atomic view of cation diffusion pathways from single-crystal topochemical transformations. *Angew. Chem. Int. Ed. Engl.* **59**, 16385–16392 (2020).
13. J. L. Andrews *et al.*, Reversible Mg-ion insertion in a metastable one-dimensional polymorph of $V_2O_5$. *Chem* **4**, 564–585 (2018).
14. Y. Zhang, K. S. R. Chandran, H. Z. Bilheux, Imaging of the Li spatial distribution within $V_2O_5$ cathode in a coin cell by neutron computed tomography. *J. Power Sources* **376**, 125–130 (2018).
15. A. Parija, D. Prendergast, S. Banerjee, Evaluation of multivalent cation insertion in single- and double-layered polymorphs of $V_2O_5$. *ACS Appl. Mater. Interfaces* **9**, 23756–23765 (2017).
16. Y. Zhao *et al.*, Modeling of phase separation across interconnected electrode particles in lithium-ion batteries. *RSC Adv.* **7**, 41254–41264 (2017).
17. L. R. De Jesus *et al.*, Striping modulations and strain gradients within individual particles of a cathode material upon lithiation. *Mater. Horiz.* **5**, 486–498 (2018).
18. G. A. Horrocks, M. F. Likely, J. M. Velazquez, S. Banerjee, Finite size effects on the structural progression induced by lithiation of $V_2O_5$: A combined diffraction and Raman spectroscopy study. *J. Mater. Chem. A* **1**, 15265–15277 (2013).
19. J. L. Andrews *et al.*, Curvature-induced modification of mechano-electrochemical coupling and nucleation kinetics in a cathode material. *Matter* **3**, 1–20 (2020).
20. D. Fraggedakis *et al.*, A scaling law to determine phase morphologies during ion intercalation. *Energy Environ. Sci.* **13**, 2142–2152 (2020).
21. D. A. Cogswell, M. Z. Bazant, Coherency strain and the kinetics of phase separation in $LiFePO_4$ nanoparticles. *ACS Nano* **6**, 2215–2225 (2012).
22. Y. Luo *et al.*, Roadblocks in cation diffusion pathways: Implications of phase boundaries for Li-ion diffusivity in an intercalation cathode material. *ACS Appl. Mater. Interfaces* **10**, 30901–30911 (2018).
23. L. R. De Jesus *et al.*, Mapping polaronic states and lithiation gradients in individual $V_2O_5$ nanowires. *Nat. Commun.* **7**, 12022 (2016).
24. H. J. Noh, S. Youn, C. S. Yoon, Y. K. Sun, Comparison of the structural and electrochemical properties of layered $Li[NixCoyMnz]O_2$ (x = 1/3, 0.5, 0.6, 0.7, 0.8 and 0.85) cathode material for lithium-ion batteries. *J. Power Sources* **233**, 121–130 (2013).
25. H. Li *et al.*, Is cobalt needed in Ni-rich positive electrode materials for lithium ion batteries? *J. Electrochem. Soc.* **166**, A429–A439 (2019).
26. Y. Bai, K. Zhao, Y. Liu, P. Stein, B. X. Xu, A chemo-mechanical grain boundary model and its application to understand the damage of Li-ion battery materials. *Scr. Mater.* **183**, 45–49 (2020).
27. F. Zhou, C. A. Marianetti, M. Cococcioni, D. Morgan, G. Ceder, Phase separation in $Li_xFePO_4$ induced by correlation effects. *Phys. Rev. B Condens. Matter Mater. Phys.* **69**, 1–4 (2004).

28. F. Xin *et al.*, What is the role of Nb in nickel-rich layered oxide cathodes for lithium-ion batteries? *ACS Energy Lett.* **6**, 1377–1382 (2021).
29. D. A. Santos *et al.*, Bending good beats breaking bad: Phase separation patterns in individual cathode particles upon lithiation and delithiation. *Mater. Horiz.* **7**, 3275–3290 (2020).
30. D. A. Cogswell, M. Z. Bazant, Theory of coherent nucleation in phase-separating nanoparticles. *Nano Lett.* **13**, 3036–3041 (2013).
31. Y. Luo *et al.*, Effect of crystallite geometries on electrochemical performance of porous intercalation electrodes by multiscale operando investigation. *Nat. Mater.*, 10.1038/s41563-021-01151-8 (2021).
32. P. M. Marley, G. A. Horrocks, K. E. Pelcher, S. Banerjee, Transformers: The changing phases of low-dimensional vanadium oxide bronzes. *Chem. Commun. (Camb.)* **51**, 5181–5198 (2015).
33. A. Parija *et al.*, Topochemically de-intercalated phases of $V_2O_5$ as cathode materials for multivalent intercalation batteries: A first-principles evaluation. *Chem. Mater.* **28**, 5611–5620 (2016).
34. G. A. Horrocks *et al.*, Mitigating cation diffusion limitations and intercalation-induced framework transitions in a 1D tunnel-structured polymorph of $V_2O_5$. *Chem. Mater.* **29**, 10386–10397 (2017).
35. N. H. Bashian *et al.*, Correlated polyhedral rotations in the absence of polarons during electrochemical insertion of lithium in $ReO_3$. *ACS Energy Lett.* **3**, 2513–2519 (2018).
36. S. Zhou, G. Barim, B. J. Morgan, B. C. Melot, R. L. Brutchey, Influence of rotational distortions on $Li^+$- and $Na^+$-intercalation in anti-NASICON $Fe_2(MoO_4)_3$. *Chem. Mater.* **28**, 4492–4500 (2016).
37. A. Pan, H. B. Wu, L. Yu, X. W. Lou, Template-free synthesis of $VO_2$ hollow microspheres with various interiors and their conversion into $V_2O_5$ for lithium-ion batteries. *Angew. Chem. Int. Ed. Engl.* **52**, 2226–2230 (2013).
38. A. M. Cao, J. S. Hu, H. P. Liang, L. J. Wan, Self-assembled vanadium pentoxide ($V_2O_5$) hollow microspheres from nanorods and their application in lithium-ion batteries. *Angew. Chem. Int. Ed. Engl.* **44**, 4391–4395 (2005).
39. C. K. Christensen, D. R. Sørensen, J. Hvam, D. B. Ravnsbæk, Structural evolution of disordered $Li_xV_2O_5$ bronzes in $V_2O_5$ cathodes for Li-ion batteries. *Chem. Mater.* **31**, 512–520 (2019).
40. T. Rajendra *et al.*, Quantifying transport, geometrical, and morphological parameters in Li-ion cathode phases using X-ray microtomography. *ACS Appl. Mater. Interfaces* **11**, 19933–19942 (2019).
41. P. Rozier *et al.*, $\varepsilon$-Lix $V_2O_5$ bronzes ($033 \leq X \leq 064$) a joint study by X-ray powder diffraction and 6 Li, 7 Li MAS NMR. *Eur. J. Solid State Inorg. Chem.* **33**, 1–13 (1996).
42. D. W. Murphy, P. A. Christian, F. J. Disalvo, J. V. Waszczak, Lithium incorporation by vanadium pentoxide. *Inorg. Chem.* **18**, 2800–2803 (1979).
43. A. P. Hitchcock, Soft X-ray spectromicroscopy and ptychography. *J. Electron Spectrosc. Relat. Phenom.* **200**, 49–63 (2015).
44. M. Wolf, B. M. May, J. Cabana, Visualization of electrochemical reactions in battery materials with X-ray microscopy and mapping. *Chem. Mater.* **29**, 3347–3362 (2017).
45. D. Maganas *et al.*, First principles calculations of the structure and V L-edge X-ray absorption spectra of $V_2O_5$ using local pair natural orbital coupled cluster theory and spin-orbit coupled configuration interaction approaches. *Phys. Chem. Chem. Phys.* **15**, 7260–7276 (2013).
46. L. R. De Jesus *et al.*, Lithiation across interconnected $V_2O_5$ nanoparticle networks. *J. Mater. Chem. A* **5**, 20141–20152 (2017).
47. Y. Zhao *et al.*, A review on modeling of electro-chemo-mechanics in lithium-ion batteries. *J. Power Sources* **413**, 259–283 (2019).
48. J. A. Lewis, J. Tippens, F. J. Q. Cortes, M. T. McDowell, Chemo-mechanical challenges in solid-state batteries. *Trends Chem.* **1**, 845–857 (2019).
49. N. Muralidharan *et al.*, Tunable mechanochemistry of lithium battery electrodes. *ACS Nano* **11**, 6243–6251 (2017).
50. Y. Zhang, Y. Luo, C. Fincher, S. Banerjee, M. Pharr, Chemo-mechanical degradation in $V_2O_5$ thin film cathodes of Li-ion batteries during electrochemical cycling. *J. Mater. Chem.* **7**, 23922–23930 (2019).
51. Z. Qi *et al.*, Enhancing electrochemical performance of thin film lithium ion battery via introducing tilted metal nanopillars as effective current collectors. *Nano Energy* **69**, 104381 (2020).
52. Z. Rong *et al.*, Materials design rules for multivalent ion mobility in intercalation structures. *Chem. Mater.* **27**, 6016–6021 (2015).
53. G. S. Gautam *et al.*, First-principles evaluation of multi-valent cation insertion into orthorhombic $V_2O_5$. *Chem. Commun. (Camb.)* **51**, 13619–13622 (2015).
54. T. M. Tolhurst *et al.*, Contrasting 1D tunnel-structured and 2D layered polymorphs of $V_2O_5$: Relating crystal structure and bonding to band gaps and electronic structure. *Phys. Chem. Chem. Phys.* **18**, 15798–15806 (2016).
55. G. A. Horrocks, L. R. De Jesus, J. L. Andrews, S. Banerjee, X-ray spectroscopy and imaging as multiscale probes of intercalation phenomena in cathode materials. *JOM* **69**, 1469–1477 (2017).
56. O. J. Borkiewicz *et al.*, The AMPIX electrochemical cell: A versatile apparatus for in situ X-ray scattering and spectroscopic measurements. *J. Appl. Cryst.* **45**, 1261–1269 (2012).
57. B. H. Toby, R. B. Von Dreele, GSAS-II: The genesis of a modern open-source all purpose vrystallography software package. *J. Appl. Cryst.* **46**, 544–549 (2013).
58. Y. Zhang *et al.*, In-situ measurements of stress evolution in composite sulfur cathodes. *Energy Storage Mater.* **16**, 491–497 (2018).